Supplementary Materials

Microcavity-assisted multi-resonant metasurfaces enabling versatile wavefront engineering

Shih-Hsiu Huang[1], Hsiu-Ping Su[1], Chao-Yun Chen[1], Yu-Chun Lin[1], Zijin Yang[2], Yuzhi Shi[3*], Qinghua Song[2*], and Pin Chieh Wu[1,4,5*]

[1]Department of Photonics, National Cheng Kung University, Tainan 70101, Taiwan

[2]Tsinghua Shenzhen International Graduate School, Tsinghua University, Shenzhen, 518055, China

[3]Institute of Precision Optical Engineering, School of Physics Science and Engineering, Tongji University, Shanghai 200092, China

[4]Center for Quantum Frontiers of Research & Technology (QFort), National Cheng Kung University, Tainan, 70101, Taiwan

[5]Meta-nanoPhotonics Center, National Cheng Kung University, Tainan, 70101, Taiwan

*E-mail address: yzshi@tongji.edu.cn; song.qinghua@sz.tsinghua.edu.cn; pcwu@gs.ncku.edu.tw

Supplementary Note 1. Correlation of resonances in MIM metasurfaces and an FP cavity

In the case of an MIM metasurface, the optical response primarily depends on the geometric dimensions of the topmost nanostructure when the thickness of the dielectric spacer remains constant. **Supplementary Figures 3a** and **3d** represent the simulated LCP-to-RCP conversion efficiency spectrum for two MIM metasurfaces with different physical dimensions. It is evident that the efficiency of conversion is highly sensitive to the geometric sizes of the nanostructures. Conversely, the reflection intensity for FP cavities remains nearly constant across the same spectral range, as shown in **Supplementary Figures 3b** and **3e**. Notably, the variation in reflection for high-Q resonance peaks in the multi-resonant high-Q metasurfaces demonstrates a nearly linear correlation with the combined reflection intensity from the MIM metasurface and the FP microcavity (refer to **Supplementary Figures 3c** and **3f**).

Supplementary Note 2. Analytical model for an MIM metasurface

For an MIM metasurface, where all wavelengths share the same cavity dielectric thickness, its spectral response can be analytically described using a multilayer model[1]. To theoretically predict the peak wavelengths of the MIM metasurface (see Fig. 2a in the main article), which consists of an Al meta-atom, a SiO_2 dielectric spacer, and an Al mirror from top to bottom, we first numerically simulate the transmission spectrum of the Al meta-atom on a SiO_2 substrate. The physical dimensions of the Al meta-atom are identical to those shown in Fig. 2a. Based on the multilayer model, the transmission coefficient t_i of the meta-atom under *i*-polarized illumination is expressed as:

$$t_i = 1/(\tfrac{1+n_s}{2} - i\omega P_i) \tag{S1}$$

where $P_i = -\frac{g_i}{\omega-\omega_{0i}+i\gamma_i}$ and n_s is the refractive index of the SiO_2 substrate. For simplicity, n_s is set as a constant of 1.456. Here, g_i, ω_{0i}, and γ_i represent the coupling parameter, eigenfrequency, and the damping constant of the meta-atom under *i*-polarized illumination ($i = x, y$), respectively. By fitting the numerically simulated transmission spectra with Eq. (S1), as shown in **Supplementary Figures 4a** and **4b** (where the long axis of the Al meta-atom is along the *x*-axis), we extract the following parameters for the meta-atom under different linearly polarized illuminations: $g_x = 0.51648$, $\omega_{0x} = 3.59038\times10^{15}$ rad/s, $\gamma_x = 2.40651\times10^{14}$ rad/s; $g_y = 0.36957$, $\omega_{0y} = 7.84586\times10^{15}$ rad/s, $\gamma_y = 5.25536\times10^{14}$ rad/s.

Next, the reflection coefficient r_i of an MIM metasurface under *i*-polarized illumination can be calculated as:

$$r_i = -\frac{\frac{n_s-1}{2}(\omega-\omega_{0i}+i\gamma_i)+i\omega g_i-[\frac{n_s+1}{2}(\omega-\omega_{0i}+i\gamma_i)-i\omega g_i]e^{i\alpha}}{\frac{n_s+1}{2}(\omega-\omega_{0i}+i\gamma_i)+i\omega g_i-[\frac{n_s-1}{2}(\omega-\omega_{0i}+i\gamma_i)-i\omega g_i]e^{i\alpha}} \tag{S2}$$

where $\alpha = 2n_s d k_0 + \varphi(r_m)$ is the round-trip phase of the dielectric layer and the reflection phase at the metallic mirror. The complex reflection coefficient r_m, which is the complex reflection coefficient at the dielectric spacer-metal interface, can be obtained via numerical simulation when the Al meta-atom is absent. Here, d and $\varphi(r_m)$ are the thickness of SiO_2 spacer and the phase of the complex reflection coefficient r_m, respectively.

The complex electric amplitudes can be described as:

$$\begin{pmatrix} E_x^r \\ E_y^r \end{pmatrix} = \begin{pmatrix} r_x & 0 \\ 0 & r_y \end{pmatrix} \begin{pmatrix} E_x^{in} \\ E_y^{in} \end{pmatrix} \tag{S3}$$

where E_i^r and E_i^{in} represents the *i*-polarized component of reflected electric field and incident electric field, respectively. Finally, the reflection coefficient r_{x} and r_{y} can be used to calculate the complex amplitudes for the circular polarization states as:

$$\begin{aligned} \begin{pmatrix} E_{LCP}^r \\ E_{RCP}^r \end{pmatrix} &= \frac{1}{2} \begin{pmatrix} 1 & i \\ 1 & -i \end{pmatrix} \begin{pmatrix} r_x & 0 \\ 0 & r_y \end{pmatrix} \begin{pmatrix} 1 & 1 \\ -i & i \end{pmatrix} \begin{pmatrix} E_{LCP}^{in} \\ E_{RCP}^{in} \end{pmatrix} \\ &= \begin{pmatrix} \frac{r_x+r_y}{2} & \frac{r_x-r_y}{2} \\ \frac{r_x-r_y}{2} & \frac{r_x+r_y}{2} \end{pmatrix} \begin{pmatrix} E_{LCP}^{in} \\ E_{RCP}^{in} \end{pmatrix} \end{aligned} \tag{S4}$$

By using Eqs. (S2) and (S4), we can analytically calculate the circular cross-polarized reflection of an MIM metasurface. As shown in **Supplementary Figures 4c** and **4d**, the modeled LCP-to-RCP reflection spectra closely match the numerically simulated spectra, validating the accuracy of the multilayer model for predicting the spectral response of an MIM metasurface, regardless of the dielectric spacer thickness. However, it is important to note that this model is valid only when the cavity dielectric thickness remains constant across all wavelengths in the operating bandwidth.

Supplementary Note 3. Multi-resonant high-*Q* metasurfaces with an optically-thick dielectric spacer

Supplementary Figure 10a shows the schematic illustration of the design for a multi-resonant metasurface. In contrast to the structural design detailed in the main article, a deliberate modification is introduced here. Specifically, the 68th to 87th dielectric layers (with the 1st layer attached to the glass substrate) within the gradient-thickness DBR mirror are intentionally removed and replaced by a 2100-nm-thick SiO_2 spacer. Because of reducing the number of dielectric layers, the high reflection band of the bare DBR mirror becomes narrower, as can be seen in the black curve in **Supplementary Figure 10b**. Upon the incorporation of an optimized plasmonic meta-atom onto the SiO_2 spacer, several high-*Q* polarization conversion peaks become evident within the high reflection band. Importantly, all these peaks adhere to the condition of the geometric phase effect, as evidenced by the blue curve in **Supplementary Figure 10b** and the corresponding color circles in **Supplementary Figure 10c**. The simulated electric field distributions at all peak wavelengths can be found in **Supplementary Figures 10d**, **10e**, and **Supplementary Figure 11**. As can be seen, standing wave-like field profiles are observable across all wavelengths, validating the design principle discussed in **Figures 1**, **2a**, and **3a**. Intriguingly, the variations in field distributions within the DBR and the 2100-nm SiO_2 spacer, serving as the cavity material, are distinctly different with changes in the incident wavelength. Specifically, the number of peaks and dips in the standing wave within the SiO_2 spacer increases as the incident wavelength undergoes a blue shift. This pattern aligns well with the characteristics of an FP cavity, where higher cavity modes are typically excited at shorter wavelengths. In contrast, the number of peaks within the DBR mirror decreases when the incident wavelength moves to smaller values. The intricate interplay between achieving high reflection and the FP cavity effect necessitates a specific light travel path within the DBR mirror. This interaction results in unexpected and complex field profiles, as shown in **Supplementary Figure 10** and **Supplementary Figure 11**. Notably, a relatively broad peak emerges initially near the interface of the DBR mirror and SiO_2 spacer. As the incident wavelength increases, this peak shifts towards regions farther from this interface. This observation aligns with findings from another multi-resonant metasurface discussed in the main article, reinforcing that the fundamental FP mode is indeed excited. This excitation is linked to the thickness of the dielectric layers within the DBR mirror, independent of the dielectric spacer's thickness.

Supplementary Note 4. Realization of arbitrary polarizations

A half-wave plate with a fast-axis orientation angle of φ has the capability to alter the handedness of circularly-polarized light and impart an opposing geometric phase of $\pm 2\varphi$. Specifically, it transforms $|L\rangle$ into $e^{i2\varphi}|R\rangle$ and $|R\rangle$ into $e^{-i2\varphi}|L\rangle$. The designed meta-atom can be regarded as a nano half-wave plate for the wavefront control. By arranging the meta-atoms with a rotation angle increment of φ_d, a phase gradient of $\pm 2\varphi_d$ per unit cell can be introduced. This gradient serves to direct the two circular polarization states to two opposite deflection angles, as described by:

$$\theta = \pm \operatorname{asin}\left(\frac{\lambda\varphi_d}{\pi p}\right) \tag{S5}$$

where λ is the wavelength of the incident light, θ is the deflected angle, and p is the period of the meta-atoms. Interleaving two lines of phase gradient metasurfaces with opposite orientation angle increments allows for the superposition of output LCP and RCP light at a specific angle. This configuration enables the generation of an arbitrary output polarization[2]:

$$|n\rangle = a_R|R\rangle + a_L e^{-i2\delta}|L\rangle \tag{S6}$$

where $|n\rangle$ is the new state of polarization, a_R and a_L are the amplitude of converted RCP and LCP beams, which can be controlled by either changing the number of LCP and RCP lines or adjusting the size of the meta-atoms. -2δ is the phase difference between LCP and RCP light beams which is induced by the orientation angle difference between two lines.

Based on the construction of arbitrary-polarization-state mentioned above, the amplitude distribution of LCP and RCP can be obtained by assigning different combinations of azimuth and ellipticity in the far-field:

$$A_L^f = \sqrt{[I^f - I^f \sin(2\chi^f)]/2} \tag{S7}$$

$$A_R^f = \sqrt{[I^f + I^f \sin(2\chi^f)]/2} \tag{S8}$$

where I^f is the intensity and χ^f is the ellipticity angle. In addition, the phase difference between LCP and RCP (α^f) has the following relationship with the azimuth angle ψ^f:

$$\alpha^f = 2\psi^f \tag{S9}$$

Then, a random phase (φ_{ran}) is assigned to the amplitude to gain the initial complex amplitude, and according to the modified GS algorithm, there are:

$$J_L^m(Num) = \mathcal{F}^{-1}(A_L^f e^{i\varphi_{ran}}) \tag{S10}$$

$$J_R^m(Num) = \mathcal{F}^{-1}(A_R^f e^{i\varphi_{ran}}) \tag{S11}$$

where the Num represents the number of iterations, when it is odd, we can get:

$$\begin{cases} K_R^f(Num) = \mathcal{F}(e^{i\angle[J_R^m(Num)]}) \\ J_R^m(Num+1) = \mathcal{F}^{-1}(A_R^f e^{i\angle[K_R^f(Num)]}) \\ K_L^f(Num) = \mathcal{F}(e^{i\angle[J_L^m(Num)]}) \\ J_L^m(Num+1) = \mathcal{F}^{-1}(A_L^f e^{i(\angle\left[K_R^f(Num)\right]-\alpha^f)}) \end{cases} \tag{S12}$$

And when it is even, there are:

$$\begin{cases} K_L^f(Num) = \mathcal{F}(e^{i\angle[J_L^m(Num)]}) \\ J_L^m(Num+1) = \mathcal{F}^{-1}(A_L^f e^{i\angle[K_L^f(Num)]}) \\ K_R^f(Num) = \mathcal{F}(e^{i\angle[J_R^m(Num)]}) \\ J_R^m(Num+1) = \mathcal{F}^{-1}(A_R^f e^{i(\angle\left[K_L^f(Num)\right]+\alpha^f)}) \end{cases} \tag{S13}$$

$\angle[X]$ means taking the phase value. With the above iterative algorithm, the phase information of the metasurface can be obtained:

$$\varphi_L^m(final) = \angle[J_L^m(Num_{max})] \tag{S14}$$

$$\varphi_R^m(final) = \angle[J_R^m(Num_{max})] \tag{S15}$$

The design of *x, y*-polarization is similar to above. So far, the vectorial holographic image has been successfully constructed in the far-field.

Supplementary Note 5. Relationship of imaging size with wavelength and period

The electric field in the imaging plane can be characterized by the Fourier transform of the field in the hologram plane, expressed as:

$$\begin{aligned} E(x_i, y_i) &= A\iint E(x_h, y_h)\, e^{\frac{-i2\pi(x_i x_h + y_i y_h)}{\lambda z}} dx_h dy_h \\ &= A\iint E(x_h, y_h)\, e^{-i2\pi\left(x_i\frac{x_h}{\lambda z}+y_i\frac{y_h}{\lambda z}\right)} dx_h dy_h \\ &= A\iint E\left(\frac{x_h}{\lambda z}, \frac{y_h}{\lambda z}\right) e^{-i2\pi\left(x_i\frac{x_h}{\lambda z}+y_i\frac{y_h}{\lambda z}\right)} d\left(\frac{x_h}{\lambda z}\right) d\left(\frac{y_h}{\lambda z}\right) \\ &= A\mathcal{F}\left(E\left(\frac{x_h}{\lambda z}, \frac{y_h}{\lambda z}\right)\right) \end{aligned} \tag{S16}$$

where (x_i,y_i) and (x_h,y_h) are the coordinate in the image plane and hologram plane, λ is the wavelength, k is the wavenumber, z is the propagation distance, $\mathcal{F}(\cdot)$ represents the Fourier transform. Therefore, we have:

$$E(\lambda z x_i, \lambda z y_i) = A\mathcal{F}\big(E(x_h, y_h)\big) \tag{S17}$$

It can be seen that the size of the image is directly proportional to the wavelength. The relationship of the electromagnetic field distribution in the far field and the period of the meta-atoms can be described as:

$$\begin{aligned} E(x_i, y_i) &= A\iint E\left(\frac{x_h}{\lambda z}, \frac{y_h}{\lambda z}\right) e^{-i2\pi\left(x_i\frac{x_h}{\lambda z}+y_i\frac{y_h}{\lambda z}\right)} d\left(\frac{x_h}{\lambda z}\right) d\left(\frac{y_h}{\lambda z}\right) \\ &= A\iint E\left(\frac{N_x p}{\lambda z}, \frac{N_y p}{\lambda z}\right) e^{-i2\pi\left(x_i\frac{N_x p}{\lambda z}+y_i\frac{N_y p}{\lambda z}\right)} d\left(\frac{N_x p}{\lambda z}\right) d\left(\frac{N_y p}{\lambda z}\right) \\ &= A\mathcal{F}\left(E\left(\frac{N_x p}{\lambda z}, \frac{N_y p}{\lambda z}\right)\right) \end{aligned} \tag{S18}$$

Therefore, we have:

$$E\left(\frac{\lambda z}{p} x_i, \frac{\lambda z}{p} y_i\right) = A\mathcal{F}\left(E\big(N_x, N_y\big)\right) \tag{S19}$$

where N_x and N_y are the pixels in the hologram plane. It can be seen that the size of the image is inversely proportional to the period. As a result, the relationship of the image size q along the x-direction with the wavelength λ and period p is:

$$q \propto \frac{\lambda}{p} \tag{S20}$$

i.e., if there are two metasurfaces with period of p_1 and p_2, and the corresponding wavelength of the incident light is λ_1 and λ_2, the corresponding sizes of the output holographic images have the relationship of:

$$q_1 \frac{p_1}{\lambda_1} = q_2 \frac{p_2}{\lambda_2} \tag{S21}$$

It should be noted that the image size L is the length of the image along the direction of period p. If the period in the x-direction and y-direction are different (p_x and p_y), the image size along x-direction and y-direction will be different (q_x and q_y), which satisfying the relationship of Eq. S20. Thus, the area of the images is $S = q_x q_y$. For simplicity, we set the period p as the same, so the image size is only proportional to the wavelength.

Furthermore, in order to solve the problem of compensation of image deflection angle in the case of multiple wavelengths, the translation characteristic of Fourier transform is utilized. Based on Eq. S19, the following relationship can be obtained:

$$E\big((N_{xi} - N_{x0})p_i, N_{yi}p_i\big) = A\mathcal{F}\left(E\left(\frac{N_x p}{\lambda z}, \frac{N_y p}{\lambda z}\right) . e^{i\Delta\varphi\frac{N_x p}{\lambda z}}\right) \tag{S22}$$

where N_{xi} and N_{yi} are the pixel in the image plane, N_{x0} is the pixel shift along the x-direction, p_i is the period of the image plane, and $\triangle\varphi$ is the phase gradient in the hologram between adjacent pixels along the x-direction. In the discrete Fourier transform, $\triangle\varphi$ can be represented as:

$$\Delta\varphi = -2\pi \frac{N_{x0}}{N_{x\_max}} \tag{S23}$$

where N_{x_max} is the total pixel numbers along the x-direction of the hologram/image. At this point, by constructing a reasonable image offset, holographic images at different wavelengths can be designed to the same angle, achieving image alignment under full-color conditions.

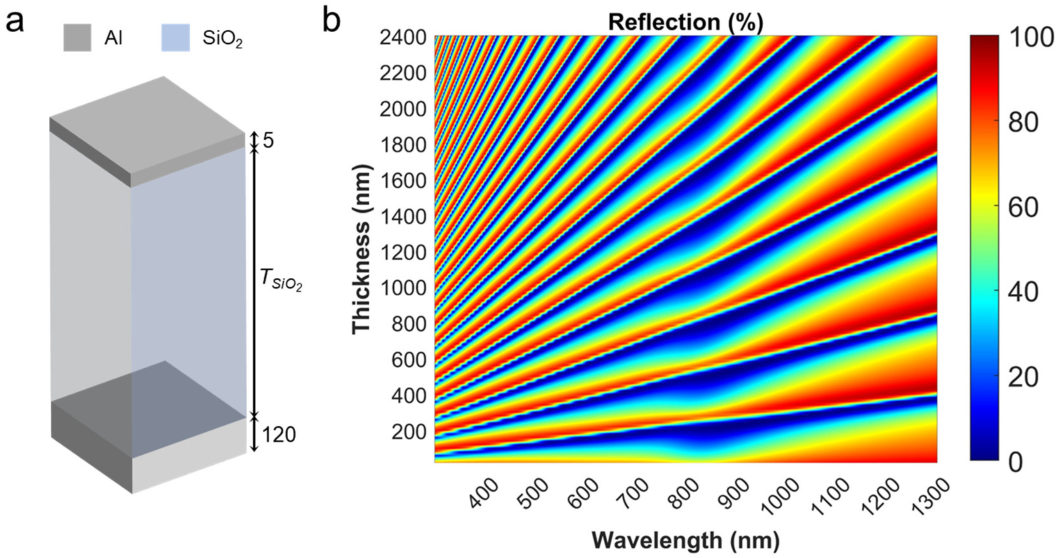

Supplementary Figure 1. Optical response of an FP cavity. (a) Schematic illustration of an FP cavity that comprises a 5-nm-thick Al thin film acting as a partially reflecting mirror and a 120-nm-thick Al mirror with full reflection. SiO_2 is used as the dielectric material for the cavity. (b) Simulated LCP-to-LCP reflection spectrum as functions of wavelength and the thickness of the SiO_2 layer.

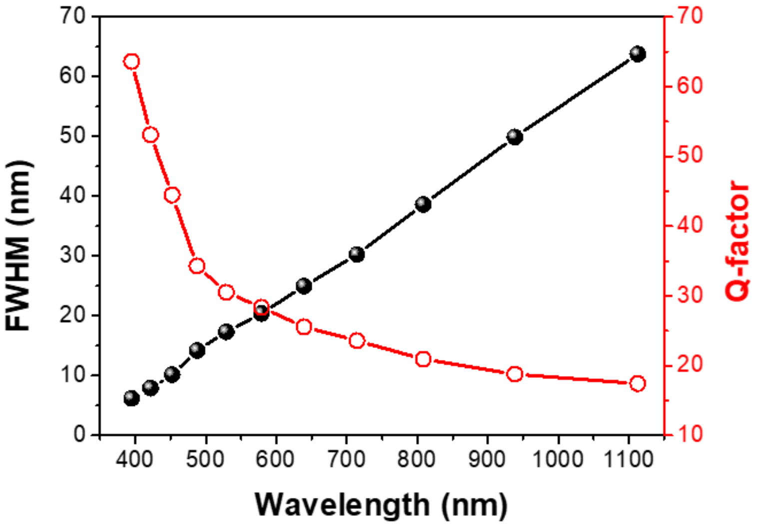

Supplementary Figure 2. Simulated FWHM and *Q*-factor of a multi-resonant metasurface. The numerically calculated FWHM and *Q*-factor at resonant peaks for a multi-resonant metasurface. The back reflector is an Al mirror. The corresponding spectrum is shown in Fig. 2c.

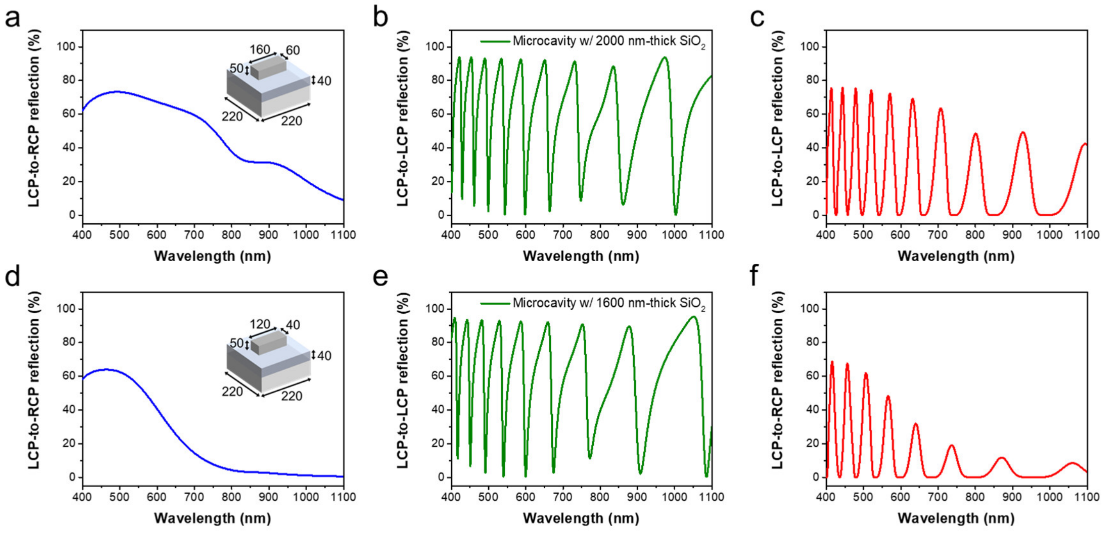

Supplementary Figure 3. Optical responses of MIM metasurfaces, FP microcavities, and multi-resonant metasurfaces. a, d LCP-to-RCP reflection spectrum of MIM metasurfaces. **b, e** LCP-to-LCP reflection spectrum of FP cavities. **c, f** LCP-to-RCP reflection spectrum of multi-resonant high-*Q* metasurfaces. The inset in a and d show the schematics and dimensions of the meta-atoms (unit: nm). Metal: Al; dielectric spacer: SiO_2.

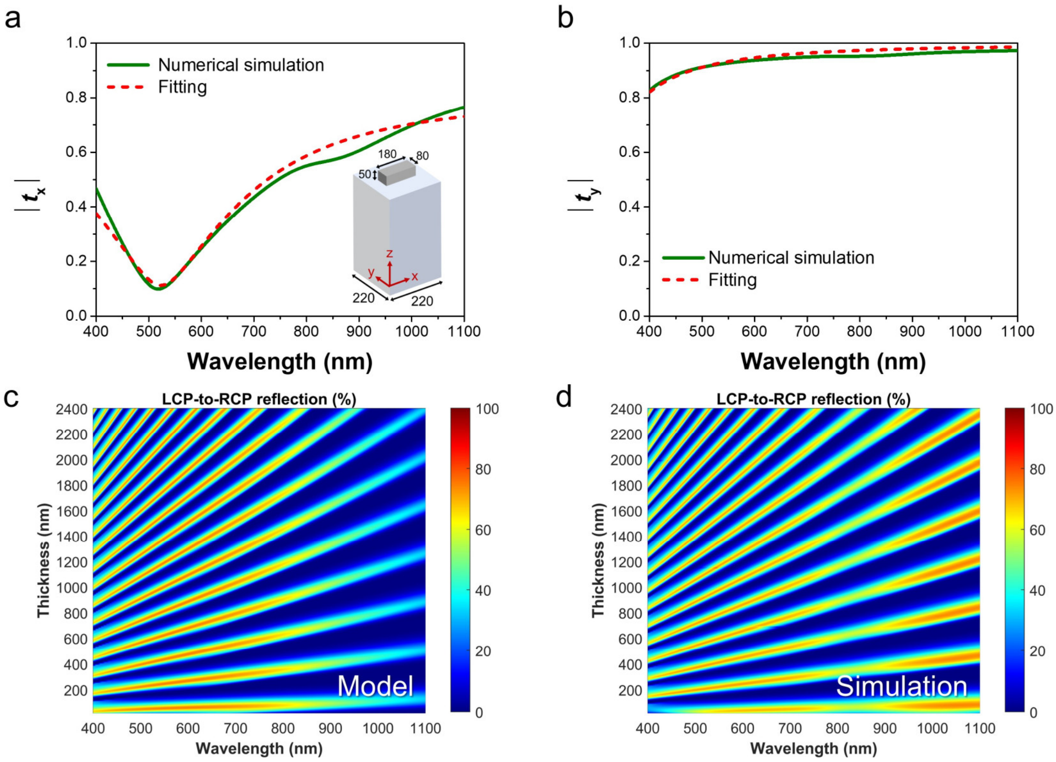

Supplementary Figure 4. Analytical calculation for an MIM metasurface. a, b Numerical simulations and theoretical calculations of the transmission amplitude for an Al meta-atom on a glass substrate, with light incident from the meta-atom side. The incident light is *x*-polarized in a and *y*-polarized in b. The inset provides a schematic of the Al meta-atom. Unit: nm. **c** Analytically modeled LCP-to-RCP reflection spectrum of the MIM metasurface with varying dielectric thicknesses. **d** Simulated LCP-to-RCP reflection spectrum of a multi-resonant high-*Q* metasurface, adapted from Fig. 2b for comparison.

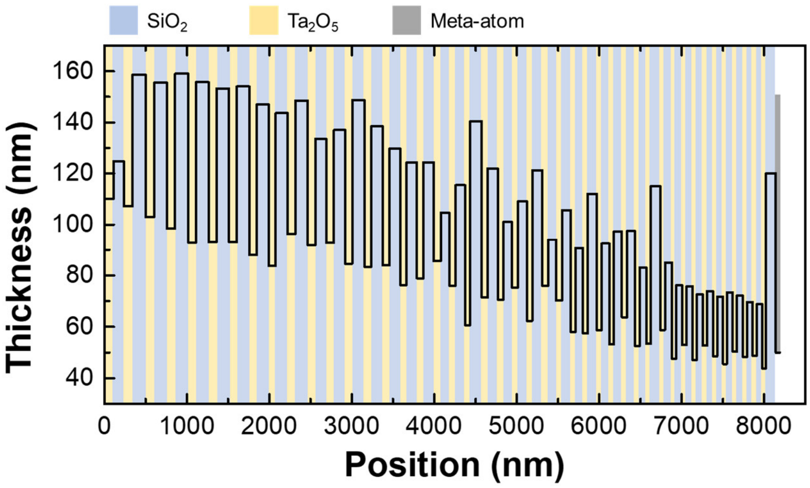

Supplementary Figure 5. Design of the gradient-thickness DBR mirror. The thickness of individual layers within the DBR mirror.

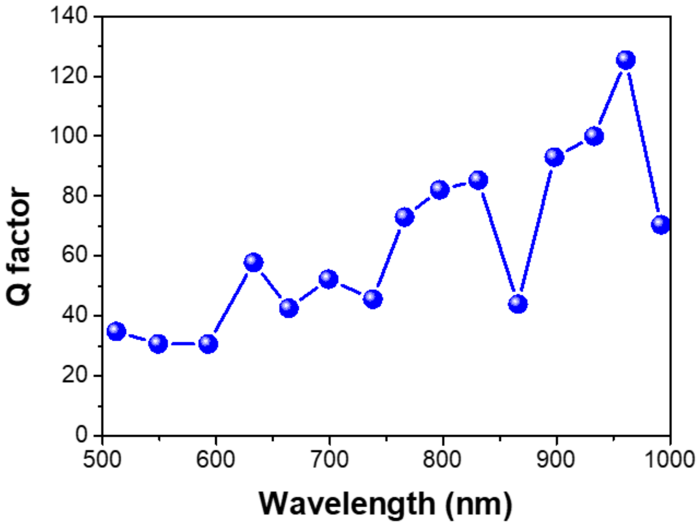

Supplementary Figure 6. *Q*-factor of a multi-resonant metasurface. The numerically calculated *Q*-factor at resonant peaks for a multi-resonant metasurface. The corresponding spectrum is shown in Fig. 3b.

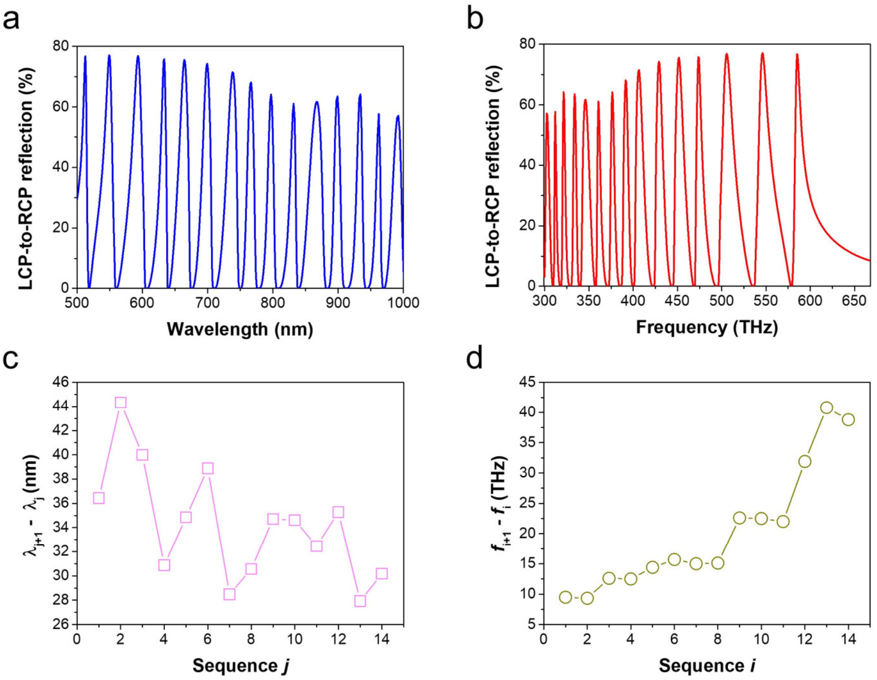

Supplementary Figure 7. Peak wavelength separation in a gradient-thickness DBR-based multi-resonant metasurface. a. The numerically calculated cross-polarized reflection of a multi-resonant metasurface, which is carried out from Fig. 3b. **b** Cross-polarized reflection plotted with frequency on the *x*-axis. **c** Wavelength difference between neighboring peaks, where λ_j represents the *j*th peak wavelength. The peak wavelengths are carried out from a. **d** Frequency difference between neighboring peaks, where f_i represents the *i*th peak frequency. The peak frequencies are carried out from b.

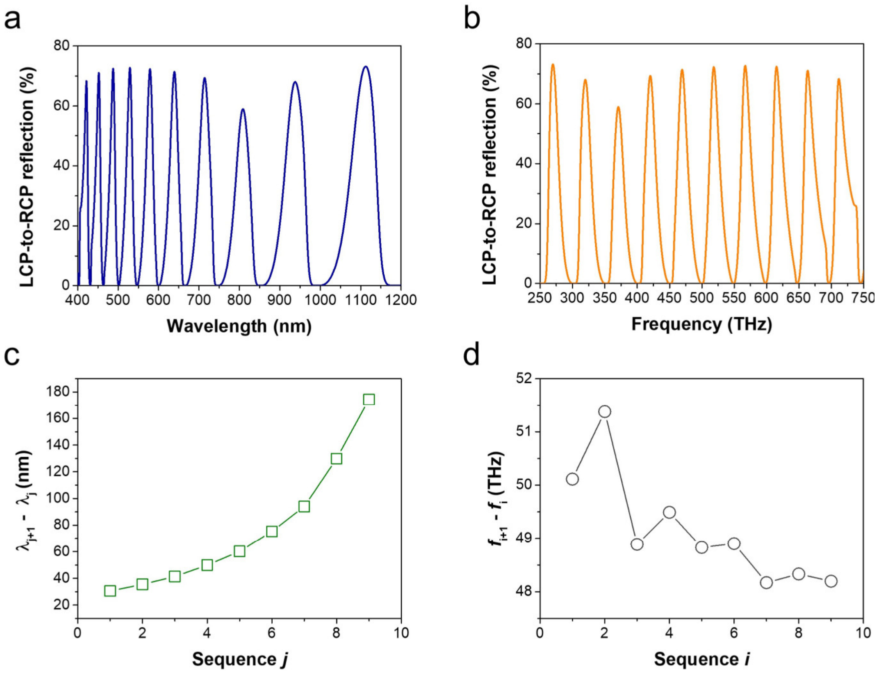

Supplementary Figure 8. Peak wavelength separation in an MIM metasurface. a. The numerically calculated cross-polarized reflection of a multi-resonant metasurface, which is carried out from Fig. 2c. **b** Cross-polarized reflection plotted with frequency on the *x*-axis. **c** Wavelength difference between neighboring peaks, where λ_j represents the *j*th peak wavelength. The peak wavelengths are carried out from a. **d** Frequency difference between neighboring peaks, where f_i represents the *i*th peak frequency. The peak frequencies are carried out from b.

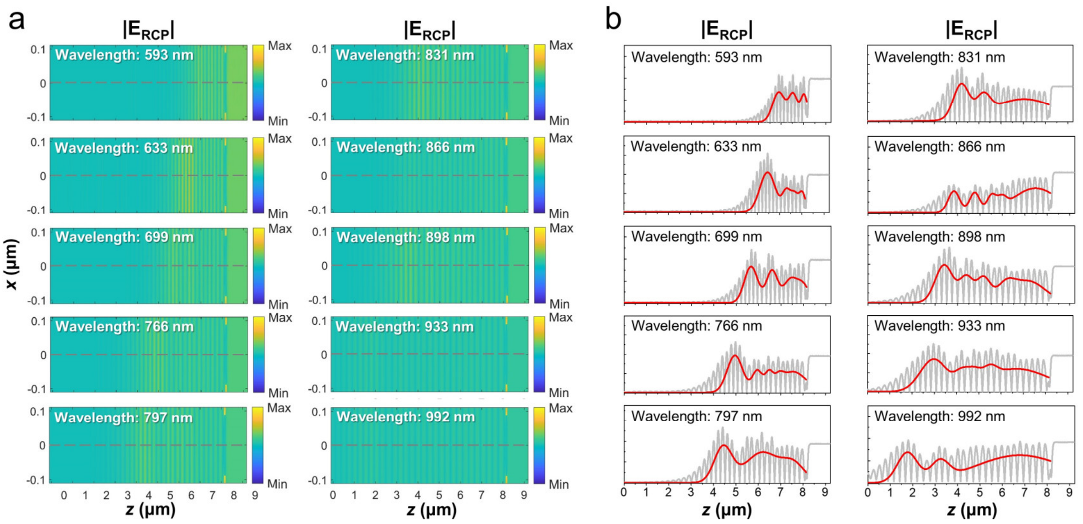

Supplementary Figure 9. Field distributions for a multi-resonant high-*Q* metasurface with an 87-layer gradient-thickness DBR. a Simulated electric field distribution of the RCP component for the multi-resonant metasurface at 10 peak wavelengths under LCP illumination. **b** Cross-sectional electric field distribution for the multi-resonant metasurface, which are extracted from the region along the red dashed lines in (a). The red curves result from multi-peak fitting for visual guidance.

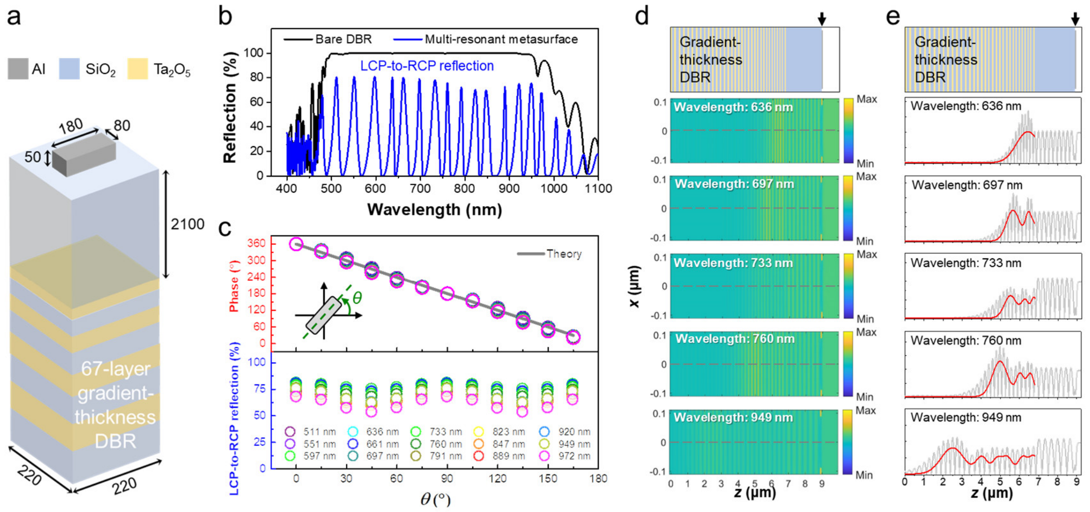

Supplementary Figure 10. Multi-resonant high-*Q* metasurface with a 67-layer gradient-thickness DBR and an optically thick dielectric layer. a Schematic illustration of a multi-resonant high-*Q* metasurface. A 2100-nm-thick SiO_2 layer is sandwiched between the nanostructure and the DBR substrate. Unit: nm. **b** Simulated LCP-to-LCP reflection spectrum (black curve) and LCP-to-RCP reflection spectrum (blue curve) for a bare 67-layer gradient-thickness DBR substrate and a multi-resonant metasurface, respectively. **c** The top panel plots LCP-to-RCP phase shift as a function of structural orientation angle high-*Q* peaks ranging from 500 nm to 1000 nm. The cross-polarized conversion efficiency with various structural angles θ is shown in the bottom panel. **d** Electric field distribution of the RCP component for the multi-resonant metasurface at 5 wavelengths under LCP illumination. **e** Cross-sectional electric field distribution for the multi-resonant metasurface, which are extracted from the region along the red dashed lines in (d). In the upper image, a schematic of the cross-sectional view is presented, with a black arrow indicating the position of the interface between the SiO_2 spacer and air. The red curves result from multi-peak fitting for visual guidance.

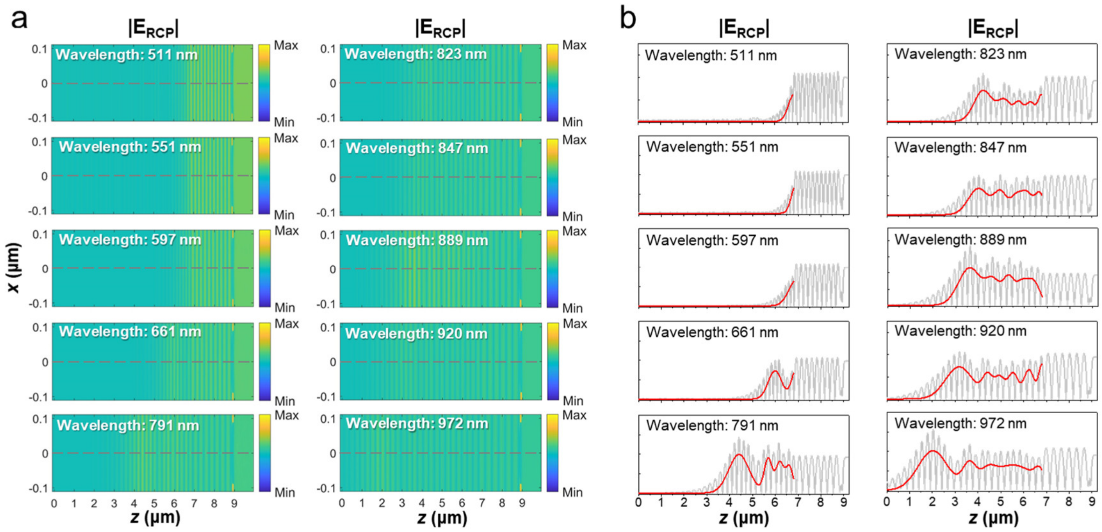

Supplementary Figure 11. Field distributions for a multi-resonant high-*Q* metasurface with a 67-layer gradient-thickness DBR and an optically thick dielectric layer. a Simulated electric field distribution of the RCP component for the multi-resonant metasurface at 10 peak wavelengths under LCP illumination. **b** Cross-sectional electric field distribution for the multi-resonant metasurface, which are extracted from the region along the red dashed lines in (a). The red curves result from multi-peak fitting for visual guidance.

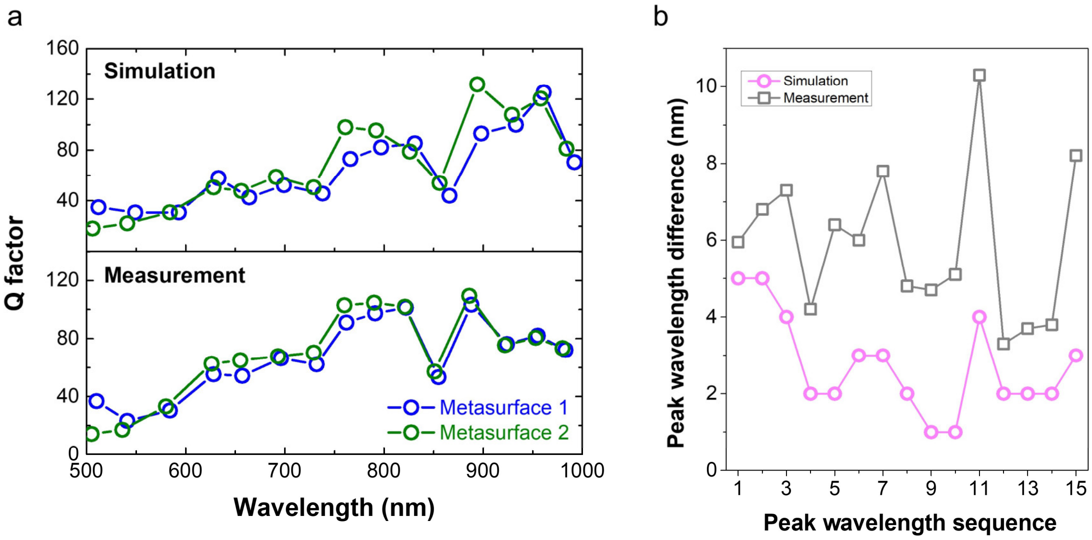

Supplementary Figure 12. Numerical and experimental characterizations of two multi-resonant metasurfaces. a The numerically calculated and experimentally measured *Q*-factor at resonant peaks for two multi-resonant metasurfaces. **b** The simulated and measured peak wavelength differences between two metasurfaces. The corresponding spectra can be found in Fig. 4b.

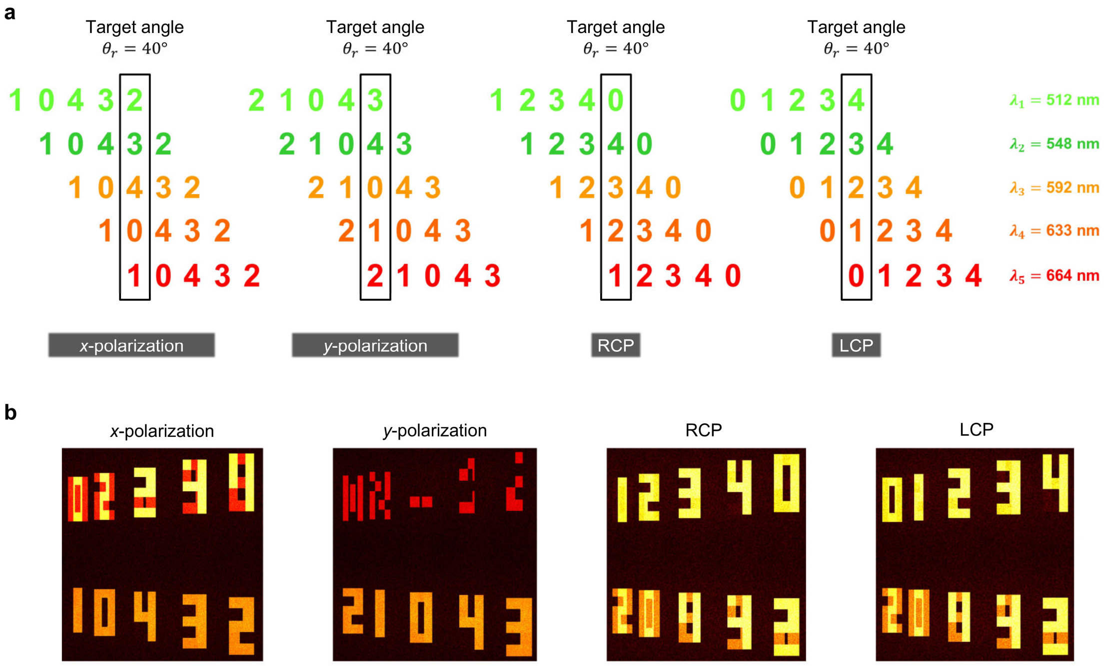

Supplementary Figure 13. Design principle of the vectorial holographic imaging for multi-channel information encryption. a Different numbers are encoded into distinct polarization channels. The five wavelength channels are predesigned into a single image with proper adjustments to size and position (see **Supplementary Note 5** for more details). The correct optical information can only be acquired when the incident wavelength, polarization state, and observation angle are all correctly aligned. For example, if the observation angle is not fixed, all the numbers "1", "0", "4", "3", and "2" can be observed when the incident wavelength is set to 512 nm and the polarization state is *x*-polarized. The designed observation angle θ_r = 40°. **b** Theoretically predicted holographic images captured under different polarization states. In practical demonstrations, linearly polarized holographic images are spatially overlapped and positioned in the bottom region of the screen, while circularly polarized holographic images are similarly overlapped but placed in the top region. Each holographic image in these polarization states contains five digits ranging from 0 to 4, with a different sequence for each polarization channel. Consequently, clear numbers can be observed when the current polarization state is examined in the far field.

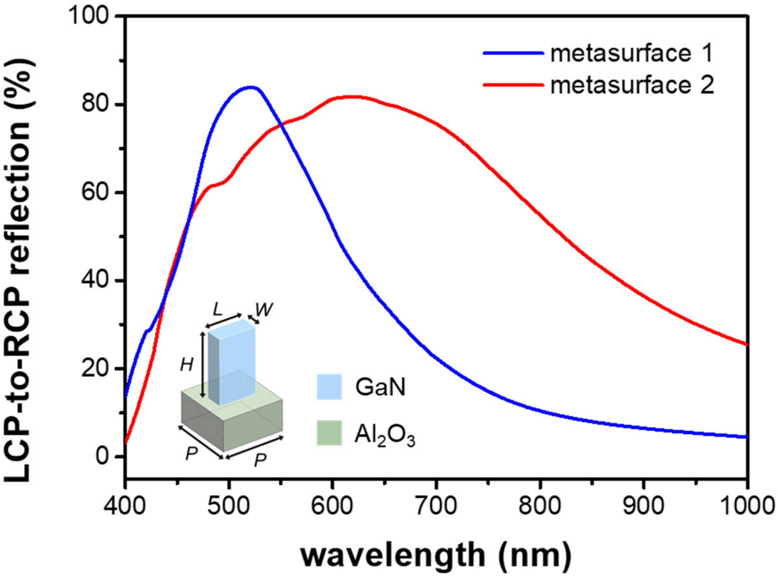

Supplementary Figure 14. Simulated cross-polarized conversion efficiency of GaN-based all-dielectric metasurface. Metasurface 1: *L* = 350 nm, *W* = 120 nm, *H* = 700 nm, and *P* = 400 nm. Metasurface 2: *L* = 260 nm, *W* = 70 nm, *H* = 700 nm, and *P* = 400 nm.

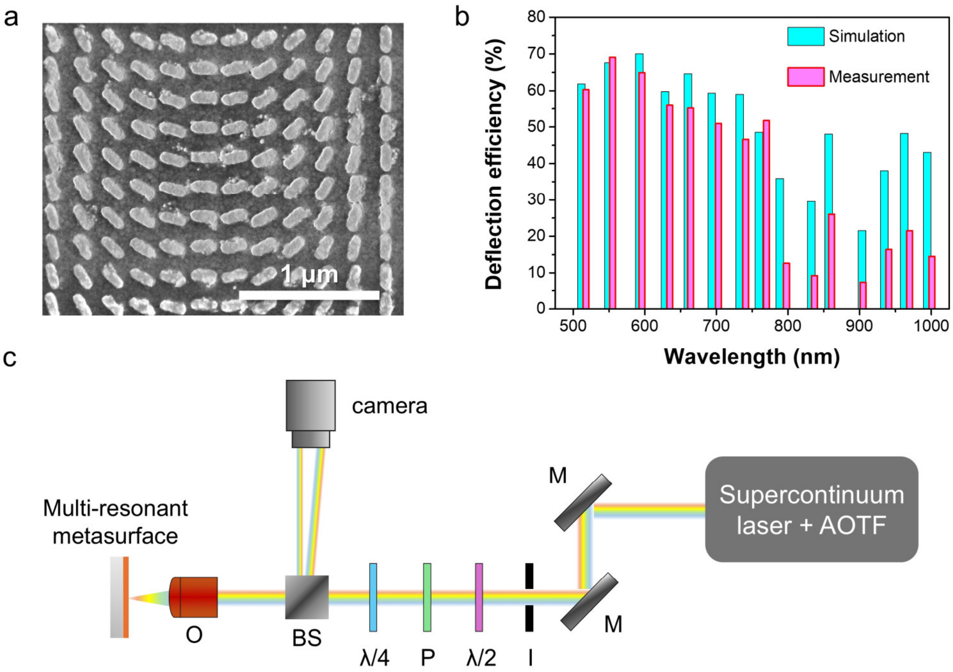

Supplementary Figure 15. Experimental demonstration of multi-resonant metasurface-based beam deflection. a An SEM image of the fabricated gradient phase metasurface. The meta-atom structure is identical to the one used in metasurface 1, as shown in Fig. 4a of the main article. The gradient phase profile was achieved using the geometric phase method. A phase level of 12 was designed for a wavelength of 633 nm, resulting in a deflection angle of 13.26°. **b** The simulated and measured beam deflection efficiencies at peak wavelengths. The deflection efficiency is defined as the ratio of the intensity of the deflected beam to the intensity of the incident light. **c** Schematic illustration of the optical setup used to characterize the beam deflection performance. To effectively capture spot images across the visible to NIR regions, a NIR-enhanced CMOS monochrome camera (CS135MU from Thorlabs) was employed. M: mirror; I: iris; $\lambda/2$: half-wave plate; $\lambda/4$: quarter-wave plate; BS: beam splitter; O: objective.

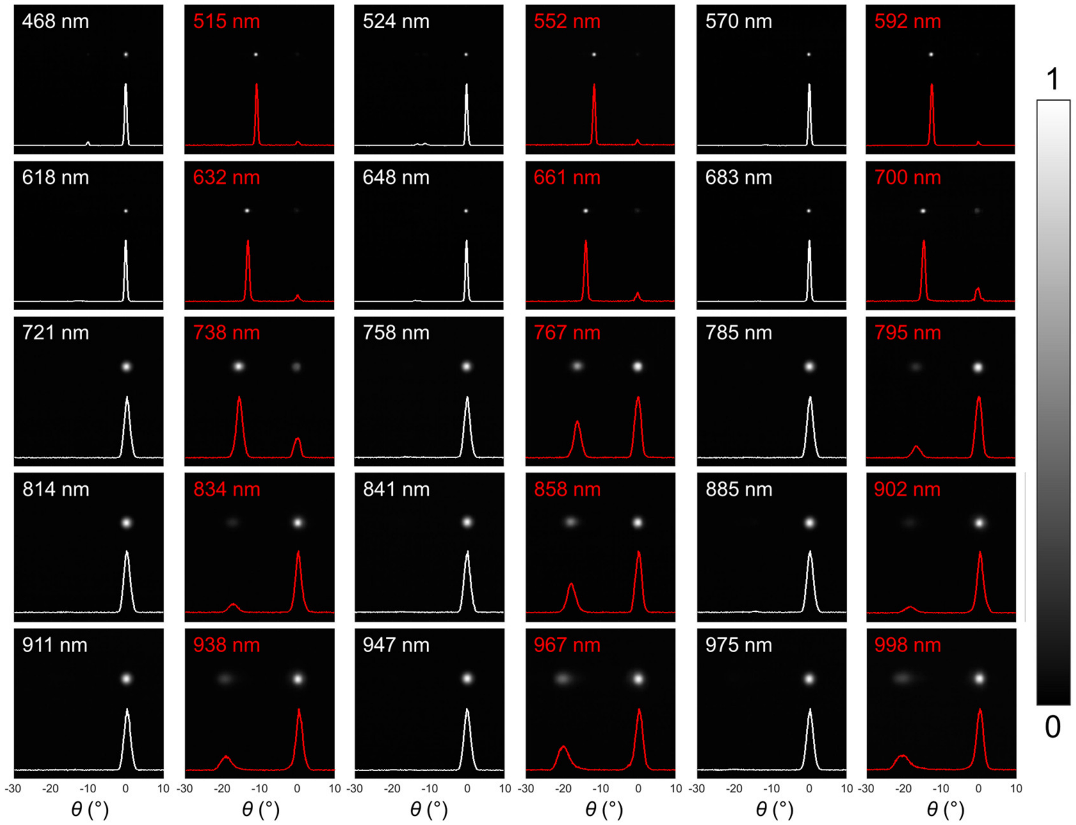

Supplementary Figure 16. Experimental verification of the broadband response of the multi-resonant metasurface. The measured Fourier images show the beam deflection achieved by the multi-resonant metasurface. Details of the sample and the optical setup used for these measurements are provided in **Supplementary Figure 15**. Since neither a polarizer nor a waveplate was placed in front of the camera, both the specular and deflected beams are visible when the incident light is LCP. The white numbers indicate the dip wavelengths, while the red numbers denote the peak wavelengths. As shown, the deflected beams are observed only at the peak wavelengths. More importantly, the beam deflection effect is evident across a broad spectral range, demonstrating that the multi-resonant metasurface can manipulate the wavefront at all peak wavelengths, extending from the visible to the NIR regions.

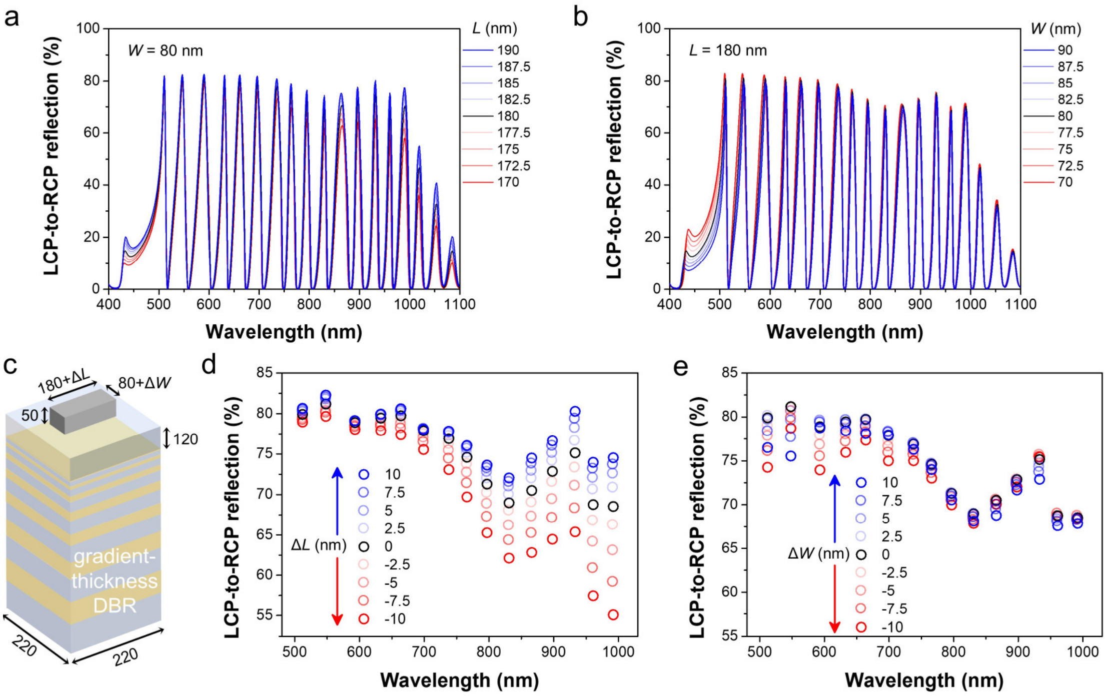

Supplementary Figure 17. Optical response due to physical size variations. a Simulated LCP-to-RCP reflection under conditions where the width of the meta-atom varies by ±10 nm, while the length is kept constant at 180 nm. **b** Simulated LCP-to-RCP reflection under conditions where the length of the meta-atom varies by ±10 nm, while the width is fixed at 80 nm. **c** Schematic illustration of the metasurface structure. **d** Peak intensity variation as a function of wavelength corresponding to a ±10 nm variation in the length of the meta-atom. **e** Peak intensity variation as a function of wavelength corresponding to a ±10 nm variation in the width of the meta-atom.

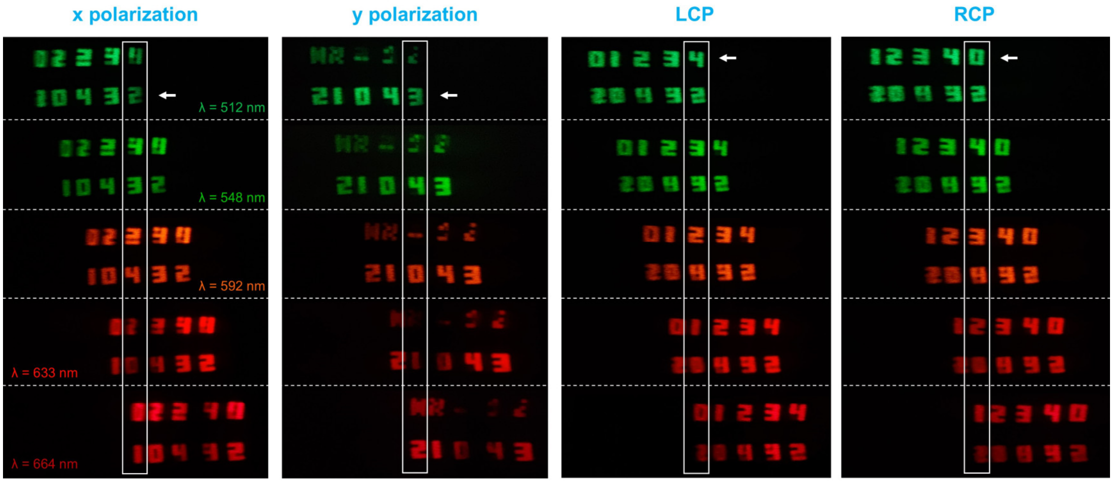

Supplementary Figure 18. Experimentally captured vectorial holographic images. The experimentally observed vectorial holographic images on the screen at different incident wavelengths and detected polarization states. The white rectangle indicates the designed observation angle of 40°, while the white arrow represents the row corresponding to the designed polarization channel.

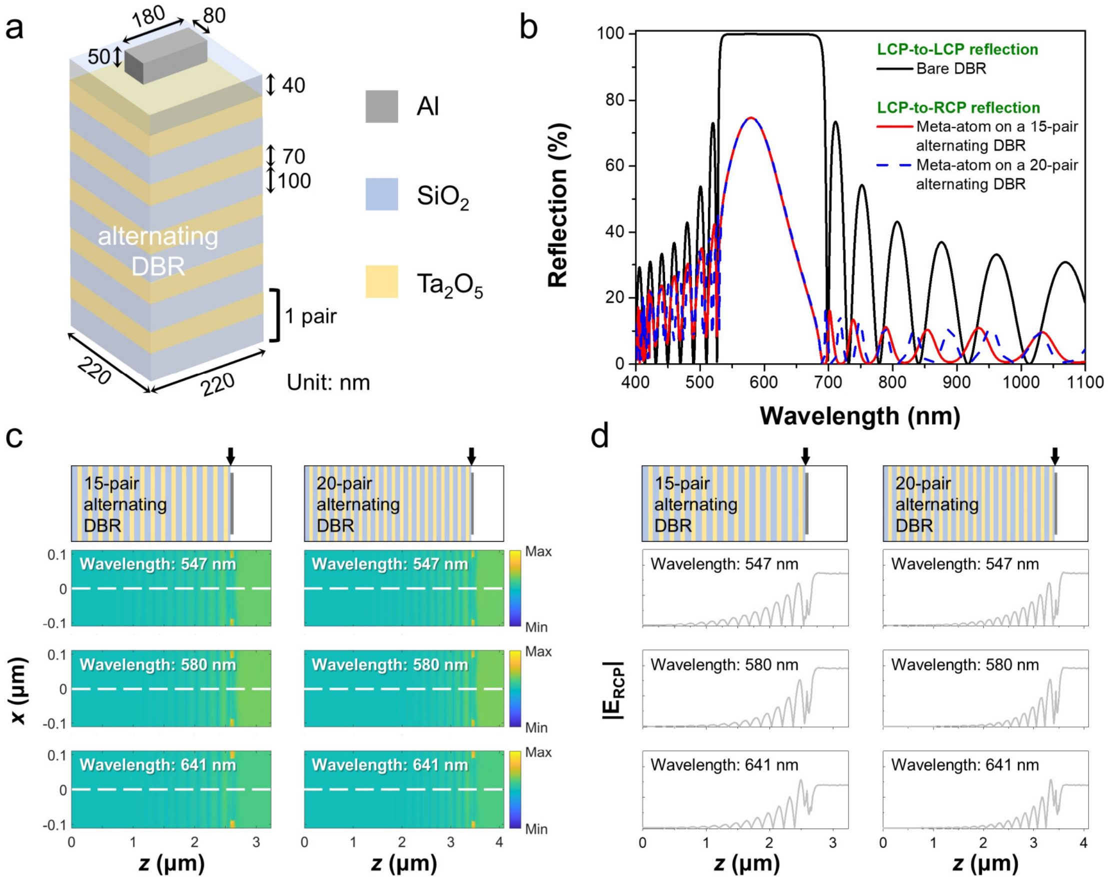

Supplementary Figure 19. Optical response of a metasurface with a conventional $\lambda/4$ DBR mirror. a Schematic illustration of the metasurface. Here, a conventional $\lambda/4$ DBR is used as the back reflector instead of a gradient-thickness DBR. **b** Simulated optical spectrum of the metasurface with different dielectric pairs inside the DBR mirror. **c** Electric field distribution of the RCP component for the metasurface at 3 wavelengths under LCP illumination. **d** Cross-sectional electric field distribution for the metasurface, which are extracted from the region along the white dashed lines in (c). In the upper image, a schematic of the cross-sectional view is presented, with a black arrow indicating the position of the interface between the meta-atom and the SiO_2 spacer.

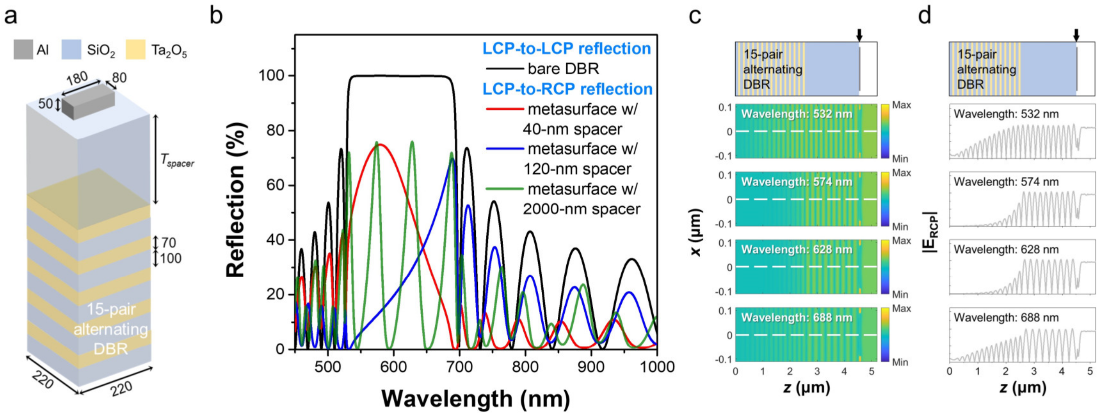

Supplementary Figure 20. Optical response of a multi-resonant metasurface with a conventional λ/4 DBR mirror centered at 610 nm. a Schematic illustration of the metasurface, where the thickness of the SiO$_2$ spacer between the meta-atom and the DBR mirror is defined as T_{spacer}. Unit: nm. **b** Simulated optical spectrum of the metasurface for varying spacer thicknesses. **c** Electric field distribution of the RCP component for the multi-resonant metasurface at 4 peak wavelengths under LCP illumination. **d** Cross-sectional electric field distribution for the multi-resonant metasurface, extracted from the region along the white dashed lines in (c). The upper image presents a schematic cross-sectional view, with a black arrow indicating the interface between the meta-atom and the SiO$_2$ spacer. For both (c) and (d), the dielectric spacer is 2000 nm thick.

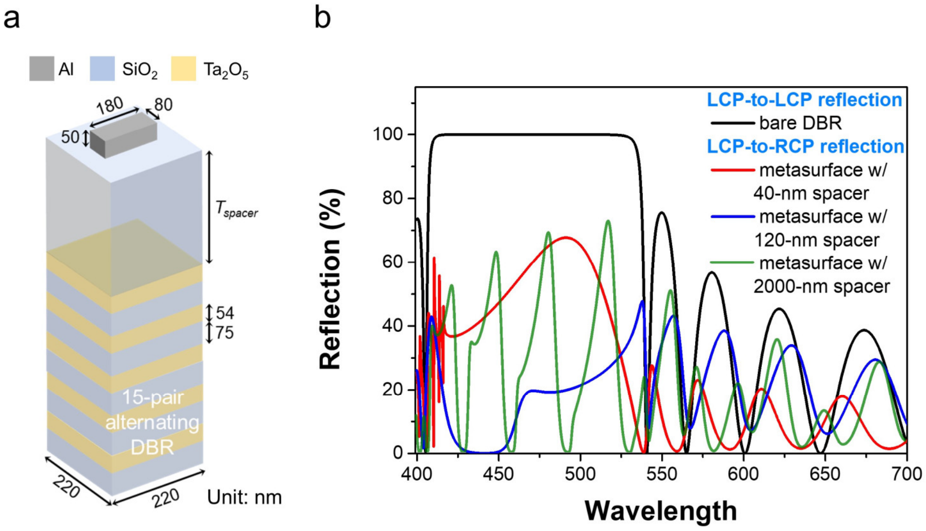

Supplementary Figure 21. Optical response of a multi-resonant metasurface with a conventional λ/4 DBR mirror centered at 470.5 nm. a Schematic illustration of the metasurface, where the thickness of the SiO_2 spacer between the meta-atom and the DBR mirror is defined as T_{spacer}. Unit: nm. **b** Simulated optical spectrum of the metasurface for varying spacer thicknesses.

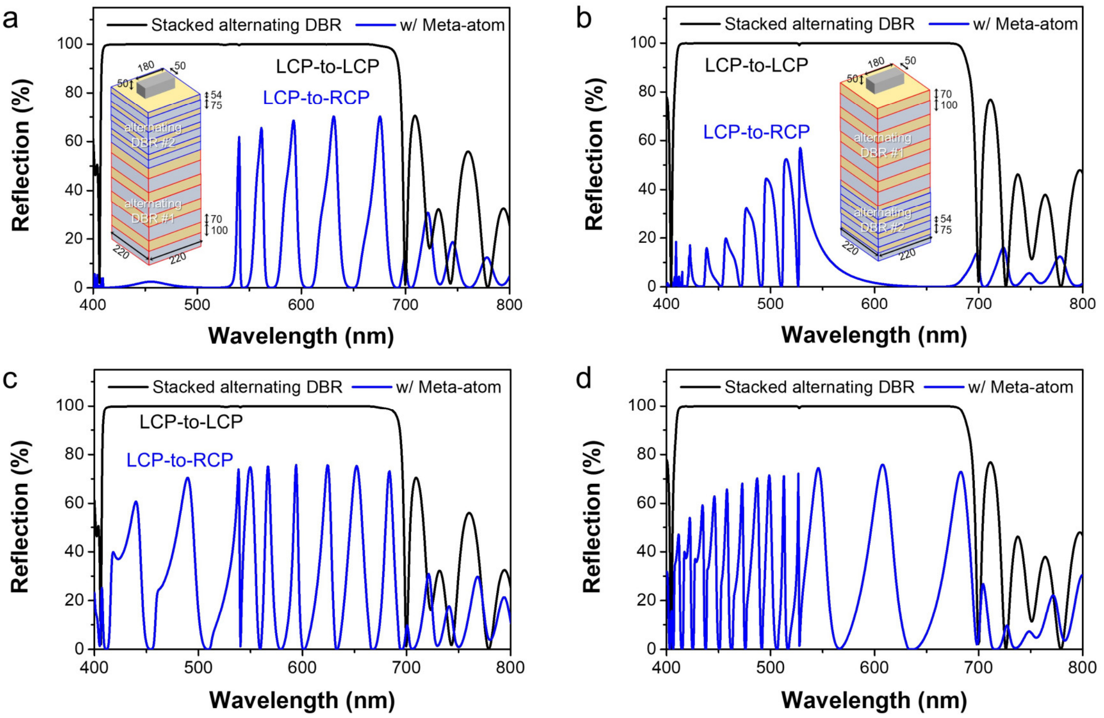

Supplementary Figure 22. Multi-resonant effect in a metasurface with a stacked alternating $\lambda/4$ DBR mirror. The simulated reflection spectrum for a stacked alternating $\lambda/4$ DBR mirror is shown for cases where the meta-atom is absent (black curve) and present (blue curve). The insets provide schematic illustrations of the structure (units: nm). The dielectric layer thicknesses for alternating DBR #1 are 70 nm for Ta_2O_5 and 100 nm for SiO_2, while for alternating DBR #2, they are 54 nm for Ta_2O_5 and 75 nm for SiO_2. **a** Alternating DBR #2 is placed on top of alternating DBR #1. **b** Alternating DBR #2 is placed below alternating DBR #1. **c** The same structural configuration as in (a), but with a 1200-nm-thick SiO_2 layer added between the meta-atom and DBR #2. **d** The same structural configuration as in (b), but with a 1200-nm-thick SiO_2 layer added between the meta-atom and DBR #1. The alternating DBR #1 and #2 are the same as demonstrated in Supplementary Figures 20 and 21, respectively.

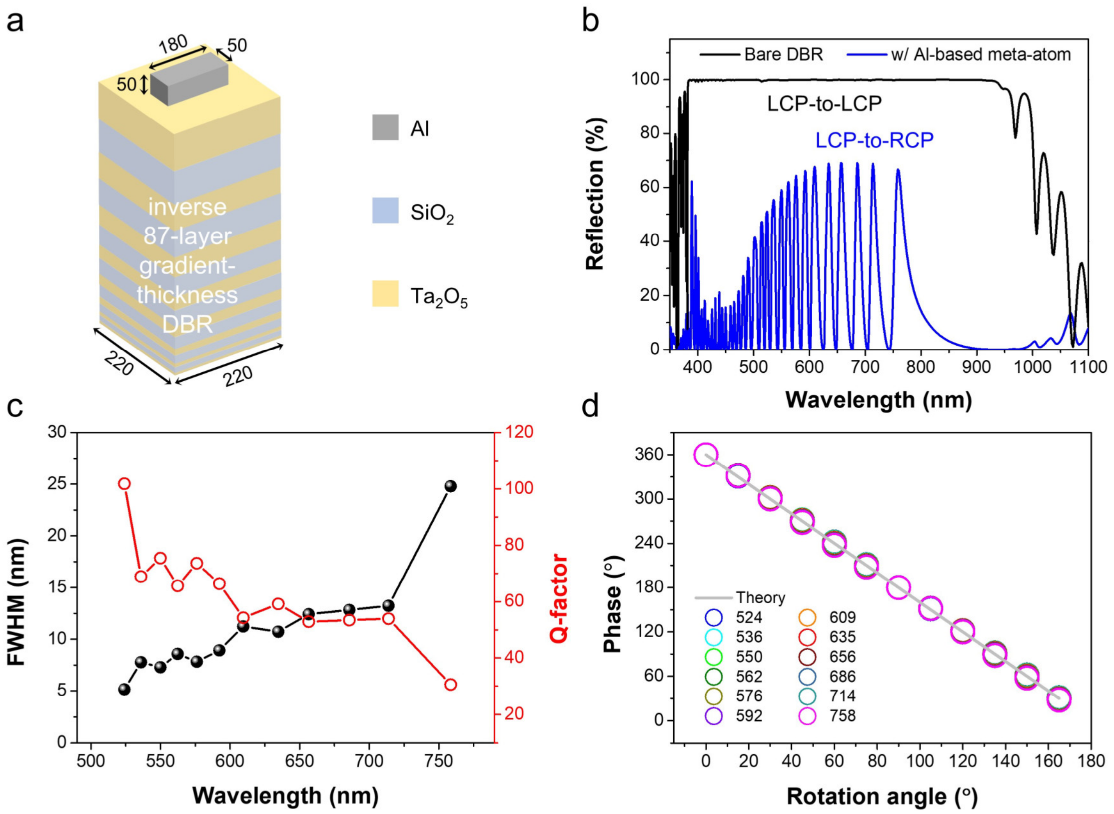

Supplementary Figure 23. Optical response of a multi-resonant metasurface with a reverse gradient-thickness DBR mirror. a Schematic illustration of the metasurface. Unit: nm. **b** Simulated optical spectrum of the bare DBR mirror (black curve) and metasurface (blue curve). **c** The numerically calculated FWHM and *Q*-factor at resonant peaks. **d** Numerical phase shift in LCP-to-RCP polarization as a function of structural orientation angle for resonant peaks.

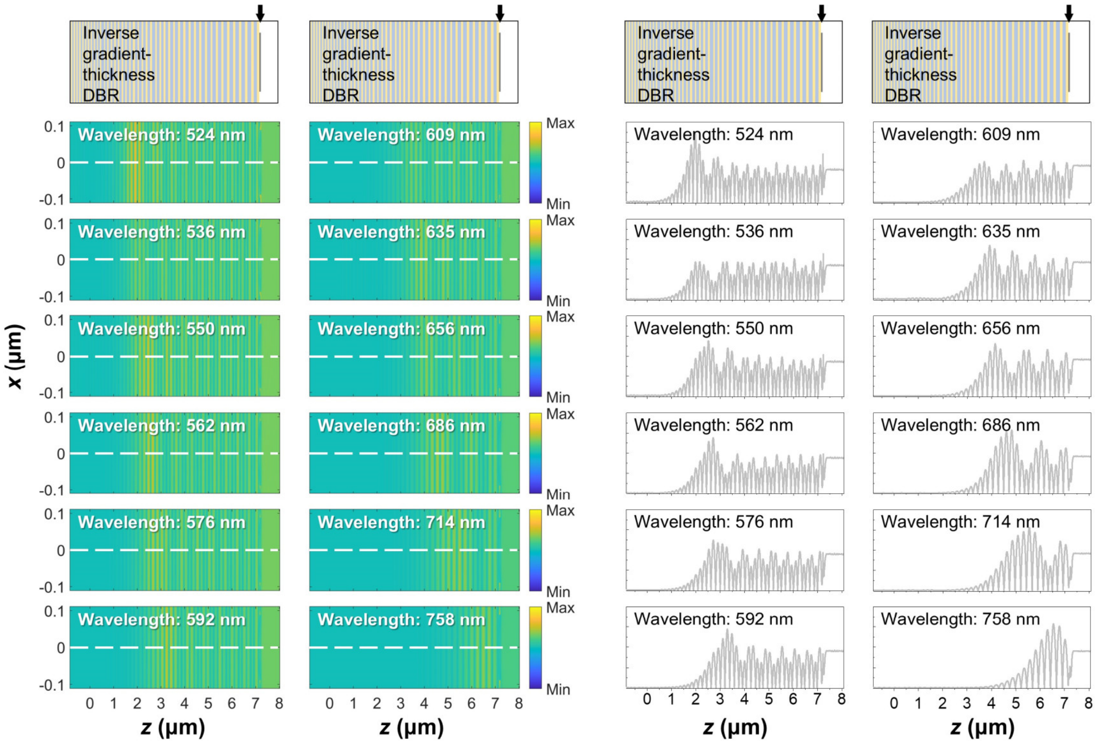

Supplementary Figure 24. Field distributions for a multi-resonant high-*Q* metasurface with a reverse gradient-thickness DBR mirror. a Simulated electric field distribution of the RCP component for the multi-resonant metasurface at 12 peak wavelengths under LCP illumination. **b** Cross-sectional electric field distribution for the multi-resonant metasurface, which are extracted from the region along the white dashed lines in (a).

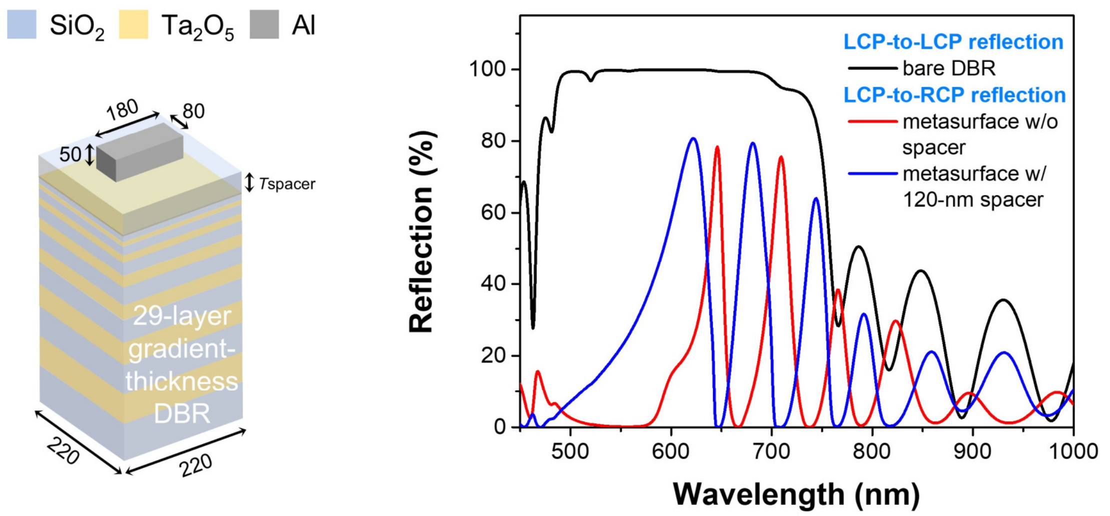

Supplementary Figure 25. Optical response of a multi-resonant metasurface with a 29-layer gradient-thickness DBR mirror. The left panel provides a schematic illustration of the metasurface (units: nm). The dielectric layers used are the 37th to 65th layers from Supplementary Figure 5, where the 1st layer is attached to the glass substrate. The right panel presents the corresponding simulated optical spectrum for both the bare DBR mirror (black curve) and the metasurface (blue and red curves). An optically thin SiO_2 spacer is inserted between the Al meta-atom and the DBR mirror to fine-tune the spectral response.

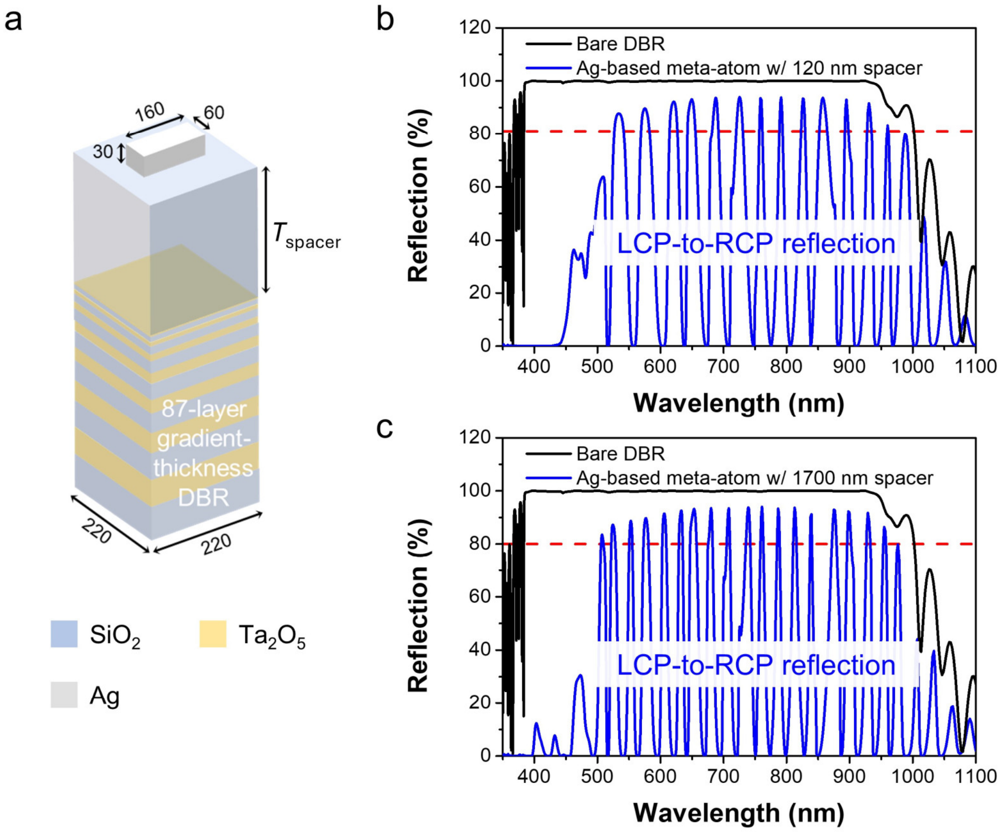

Supplementary Figure 26. Optical response of an Ag-based multi-resonant metasurface with a gradient-thickness DBR mirror. a Schematic illustration of the metasurface (units: nm). **b** Simulated LCP-to-RCP spectrum for the multi-resonant metasurface with a spacer thickness (T_{spacer}) of 120 nm. **c** Simulated LCP-to-RCP spectrum for the multi-resonant metasurface with a spacer thickness (T_{spacer}) of 1700 nm.

Supplementary Table S1. Performance comparison of our work with previous high-Q resonant metasurface designs

	Working wavelength region	Number of high-Q resonance	Multiple high-Q resonance using one single meta-atom	Amplitude modulation	Phase modulation	Wavefront engineering	Working efficiency not sensitive to the number of high-Q resonance
This work	0.5 – 1.0 μm	15	○	○	○	○	○
Ref. 3	1.4 – 1.68 μm	1	×	○	×	×	NA
Ref. 4	1.52 – 1.58 μm	2	○	○	○	○	○
Ref. 5	0.7 – 0.85 μm	1	×	○	×	×	×
Ref. 6	0.7 – 0.9 μm	2	×	○	×	×	×
Ref. 7	0.6 – 0.9 μm	2	×	○	○	○	×
Ref. 8	0.918 – 0.923 μm	2	×	○	×	×	×
Ref. 9	1.0 – 1.6 μm	7	○	○	×	×	○
Ref. 10	1.42 – 1.54 μm	1	×	○	×	×	○
Ref. 11	0.75 – 0.98 μm	1	×	○	○	○	○
Ref. 12	1.59 μm	1	×	○	○	○	○
Ref. 13	0.45 – 0.7μm	2	×	○	×	×	×
Ref. 14	0.45 – 0.7μm	3	×	×	○	○	○
Ref. 15	2.5 – 10 μm	2	×	○	×	×	×
Ref. 16	0.814 – 0.829 μm	1	×	○	×	×	×

Supplementary References

1. Zheng G., Mühlenbernd H., Kenney M., Li G., Zentgraf T., Zhang S. Metasurface holograms reaching 80% efficiency. *Nat. Nanotechnol.* **10,** 308–312 (2015).
2. Song Q., Baroni A., Sawant R., Ni P., Brandli V., Chenot S.*, et al.* Ptychography retrieval of fully polarized holograms from geometric-phase metasurfaces. *Nat. Commun.* **11,** 2651 (2020).
3. Horie Y., Arbabi A., Arbabi E., Kamali S. M., Faraon A. Wide bandwidth and high resolution planar filter array based on DBR-metasurface-DBR structures. *Opt. Express* **24,** 11677-11682 (2016).
4. Ossiander M., Meretska M. L., Rourke S., Spägele C., Yin X., Benea-Chelmus I.-C.*, et al.* Metasurface-stabilized optical microcavities. *Nat. Commun.* **14,** 1114 (2023).
5. Weber T., Kühner L., Sortino L., Ben Mhenni A., Wilson N. P., Kühne J.*, et al.* Intrinsic strong light-matter coupling with self-hybridized bound states in the continuum in van der Waals metasurfaces. *Nat. Mater.* **22,** 970-976 (2023).
6. Yang J.-H., Chen K.-P. Hybridization of plasmonic and dielectric metasurfaces with asymmetric absorption enhancement. *J. Appl. Phys.* **128,** 133101 (2020).
7. Yan C., Yang K.-Y., Martin O. J. F. Fano-resonance-assisted metasurface for color routing. *Light Sci, Appl.* **6,** e17017 (2017).
8. Baur S., Sanders S., Manjavacas A. Hybridization of lattice resonances. *ACS Nano* **12,** 1618-1629 (2018).
9. Reshef O., Saad-Bin-Alam M., Huttunen M. J., Carlow G., Sullivan B. T., Ménard J.-M.*, et al.* Multiresonant high-Q plasmonic metasurfaces. *Nano Lett.* **19,** 6429-6434 (2019).
10. Lawrence M., Barton D. R., Dixon J., Song J.-H., van de Groep J., Brongersma M. L.*, et al.* High quality factor phase gradient metasurfaces. *Nat. Nanotechnol.* **15,** 956-961 (2020).
11. McClung A., Samudrala S., Torfeh M., Mansouree M., Arbabi A. Snapshot spectral imaging with parallel metasystems. *Sci. Adv.* **6,** eabc7646 (2020).
12. Malek S. C., Overvig A. C., Alù A., Yu N. Multifunctional resonant wavefront-shaping meta-optics based on multilayer and multi-perturbation nonlocal metasurfaces. *Light Sci, Appl.* **11,** 246 (2022).
13. Shaltout A. M., Kim J., Boltasseva A., Shalaev V. M., Kildishev A. V. Ultrathin and multicolour optical cavities with embedded metasurfaces. *Nat. Commun.* **9,** 2673 (2018).
14. Li Z., Premaratne M., Zhu W. Advanced encryption method realized by secret shared phase encoding scheme using a multi-wavelength metasurface. *Nanophotonics* **9,** 3687-3696 (2020).
15. Rodrigo D., Tittl A., Ait-Bouziad N., John-Herpin A., Limaj O., Kelly C.*, et al.* Resolving molecule-specific information in dynamic lipid membrane processes with multi-resonant infrared metasurfaces. *Nat. Commun.* **9,** 2160 (2018).
16. Yesilkoy F., Arvelo E. R., Jahani Y., Liu M., Tittl A., Cevher V.*, et al.* Ultrasensitive hyperspectral imaging and biodetection enabled by dielectric

metasurfaces. *Nat. Photon.* **13,** 390-396 (2019).